Published in final edited form as:
Multiscale Model Simul. 2008 January 27; 7(2): 888–909. doi:10.1137/07070231X.

BLOOD FLOW IN THE CIRCLE OF WILLIS: MODELING AND CALIBRATION*

KRISTEN DEVAULT[†], **PIERRE A. GREMAUD**[†], **VERA NOVAK**[‡], **METTE S. OLUFSEN**[†], **GUILLAUME VERNIÈRES**[§], and **PENG ZHAO**[‡]

[†] Department of Mathematics and Center for Research in Scientific Computation, North Carolina State University, Raleigh, NC 27695-8205 (kdevault@terpalum.umd.edu, gremaud@ncsu.edu, msolufse@ncsu.edu)

[‡] Division of Gerontology, Beth Israel Deaconess Medical Center, Harvard Medical School, Boston, MA 02215 (vnovak@bidmc.harvard.edu, pzhao1@bidmc.harvard.edu)

[§] Statistical and Applied Mathematical Sciences Institute (SAMSI), Research Triangle Park, NC 27709-4006 (gvernier@email.unc.edu)

Abstract

A numerical model based on one-dimensional balance laws and ad hoc zero-dimensional boundary conditions is tested against experimental data. The study concentrates on the circle of Willis, a vital subnetwork of the cerebral vasculature. The main goal is to obtain efficient and reliable numerical tools with predictive capabilities. The flow is assumed to obey the Navier–Stokes equations, while the mechanical reactions of the arterial walls follow a viscoelastic model. Like many previous studies, a dimension reduction is performed through averaging. Unlike most previous work, the resulting model is both calibrated and validated against in vivo data, more precisely transcranial Doppler data of cerebral blood velocity. The network considered has three inflow vessels and six outflow vessels. Inflow conditions come from the data, while outflow conditions are modeled. Parameters in the outflow conditions are calibrated using a subset of the data through ensemble Kalman filtering techniques. The rest of the data is used for validation. The results demonstrate the viability of the proposed approach.

Keywords

blood flow; viscoelastic arteries; fluid-structure interaction; Kalman filtering

1. Introduction

The brain is one of the vital organs in the body, and stable perfusion is essential to maintain its function. Cerebral circulation receives 15–20% of the cardiac output and is closely regulated to maintain perfusion in response to metabolic and physiological demands. The main cerebral distribution center for blood flow is the circle of Willis (see [15,37]), a ring-like network of collateral vessels; see Figure 1(left).[1] Blood is delivered to the brain through

*This research was initiated at and was supported by the Statistical and Applied Mathematical Sciences Institute (SAMSI), Research Triangle Park, NC 27709-4006.

http://www.siam.org/journals/mms/7-2/70231.html

[1]Throughout the text, the standard abbreviated names for the vessels are used; ACA: anterior cerebral artery, MCA: middle cerebral artery, PCA: posterior cerebral artery, ACoA: anterior communicating artery, PCoA: posterior communicating artery; see also Figure 3 and Table 2.

the two internal carotid arteries and the two vertebral arteries that join intracranially to form the basilar artery. Each of the internal carotid arteries branches to form the middle and anterior cerebral arteries, which supply blood to the front and the sides of the brain (the frontal, temporal, and parietal regions of the brain). The basilar artery bifurcates into the right and left posterior cerebral arteries, which perfuse the back of the brain (the occipital lobe, the cerebellum, and the brain stem). The ring is completed by communicating arteries that connect the posterior and anterior cerebral arteries (via the posterior communicating arteries) and the two anterior cerebral arteries (via the anterior communicating arteries).

Under normal conditions, blood flow in the communicating arteries is negligible. However, if a subject has an incomplete circle of Willis, e.g., is missing one of the main arteries or communicating arteries or is under pathological conditions such as complete or partial occlusion of one of the cerebral or carotid vessels, the flow can be redirected to perfuse deprived areas [25,26]. The ring-like structure of the circle of Willis is often incomplete or not fully developed. It has been found that in more than 50% of healthy brains [5,47,48] and in more than 80% of dysfunctional brains [58], the circle of Willis contains at least one artery that is absent or underdeveloped. The most common topological variations include missing communicating vessels, fused vessels, string-like vessels, and the presence of extra vessels [4]. These topological variations may affect the ability to maintain cerebral perfusion, which may increase the risk of stroke and transient ischemic attack in patients with atherosclerosis [38]. Limited technology exists to predict perfusion response to acute occlusion due to embolus (i.e., embolic stroke) and to chronic occlusion due to atherosclerosis (i.e., carotid or other large vessel stenosis), in particular for patients with an incomplete circle of Willis. These clinical scenarios typically occur in older patients, who have a limited ability to compensate to acute changes in blood flow and thus are at greater risk for developing an acute ischemia (stroke) or chronic hypoperfusion. The significance of these problems cannot be underestimated since stroke ranks third among the leading causes of death and is the leading cause of disability in older adults [11]. Therefore patient-specific modeling is critically important to plan and predict perfusion needs in patients with significant carotid artery stenosis who need surgical repair.

One way to assess the state of the blood flow to the brain is to use a fluid dynamic model combined with subject-specific anatomical information. Fluid dynamic models have long been used to predict blood flow dynamics in almost any section of the arterial system; see, for instance, [7,8,56] for classic studies and [12,13,28,29,64] for more recent work. A number of existing fluid dynamic models have been proposed to predict blood flow in the circle of Willis. These models include one-dimensional approaches [2,16,17,41,[40],51,61,60,66], two-dimensional approaches [25,26,44], and three-dimensional approaches [3,15,24,51,50]. Due to the complexity of the underlying problem, vessels are usually treated as rigid in three-dimensional calculations. More complex models have, however, been considered (see, for instance, [21,27,31,52]) but usually for geometries significantly simpler than the circle of Willis. On the other hand, one-and two-dimensional models allow the inclusion of fluid structure effects relatively easily but at the price of severely simplified fluid dynamics. As noted in [16], most of the above models are qualitative and should be taken some steps further to make possible patient-specific studies and thereby provide powerful clinical tools which would greatly benefit neurosurgeons and patients.

The goal of this paper is to show that proper one-dimensional models can lead to simple and reliable predictions of blood flow circulation in the circle of Willis. The present contribution differs from previous work in two essential aspects. First, the vessel walls are taken as viscoelastic, as opposed to rigid or elastic, as in most previous work; see section 2. While viscoelasticity of the arterial wall is by itself not new (see, e.g., [12]), the model considered

here includes both stress and strain relaxation.[2] Second, thorough comparison and calibration of the model to experimental results are conducted; see section 6. The original data used here was obtained using digital Doppler technology (see Figure 1(right)), MRI imaging, and noninvasive finger blood pressure measurements. Previous studies of cerebral blood flow have used MRI measurements to obtain detailed patient-specific geometries (e.g., [15,50]). However, patient-specific information was not used to obtain the remaining model parameters. This is done here through ensemble Kalman filtering (see section 5), which is used to calibrate various computational boundary conditions; see section 3. To the authors' knowledge, combining fluid dynamic simulations for arterial networks with parameter identification methodology is fairly new. As such, it provides one more step toward patient-specific predictive models as set forth by Charbel et al. [16].

The rest of the proposed approach is relatively standard and is based on conservation of mass and momentum; see section 2. In each vessel, a system of balance laws has to be solved. When compared to elastic models (see, e.g., [2]), the present system has an additional equation per vessel. The computational domain is linked to the rest of the vascular system through boundary conditions as described in section 3, where the conditions at vessel bifurcations are also discussed. Discretization techniques are introduced in section 4.

2. Derivation of the model

The following assumptions are semistandard in one-dimensional hemodynamics and are adopted here:

- the blood density is constant;
- the blood flow is axisymmetric and no has no swirl;
- the vessels are tethered in their longitudinal direction;
- the equations are expressed in terms of variables averaged on cross-sections.

Further, the flow is assumed to obey to the incompressible Navier–Stokes equations

$$\rho(\partial_t \mathbf{u} + \mathbf{u} \cdot \nabla \mathbf{u}) - \nabla \cdot \boldsymbol{\sigma} = \rho \mathbf{g}, \tag{2.1}$$

$$\nabla \cdot \mathbf{u} = 0, \tag{2.2}$$

where ρ is the density, $\mathbf{u}$ is the velocity, $\boldsymbol{\sigma}$ is the stress tensor, and $\mathbf{g}$ is the acceleration due to gravity. The stress tensor is $\boldsymbol{\sigma} = -p\,\mathbb{I} + 2\mu\varepsilon$, where p is the pressure, $\varepsilon = \frac{1}{2}(\nabla \mathbf{u} + \nabla \mathbf{u}^T)$ is the strain rate tensor, and μ is the dynamic viscosity. Although not done here, the possible non-Newtonian behavior of blood can be accounted for by letting μ depend on ε; see section 7, Conclusions. However, in the present study, the constant values $\mu = 4.50$ g s^{-1} cm^{-1} for the dynamic viscosity and $\rho = 1.055$ g/cm^3 for the density were used.

Each vessel is assumed to be axisymmetric with a variable diameter. In each individual vessel, cylindrical coordinates (r, θ, x) are used with x being the distance on the longitudinal axis. Further, the shape of each axisymmetric vessel is described by a function R such that

[2] In a previous study [65], we showed that for most of the larger arteries, including the carotid artery, it is not possible to accurately predict pressure as a function of area without accounting for both of those factors.

$R(x, t)$ is the actual radius of the vessel at the point x on the x-axis at time t. Using those coordinates and the above assumptions, the velocity is $\mathbf{u} = \langle u_r, 0, u_x \rangle$.[3]

The mechanical reactions of the arterial walls are assumed to follow the viscoelastic law corresponding to the Kelvin model (see [30])

$$p - p_0 + \tau_\sigma \partial_t p = \frac{Eh}{r_0}(s + \tau_\varepsilon \partial_t s), \tag{2.3}$$

where $s = 1 - \sqrt{\frac{A_o}{A}}$ (see [65]), $A = \pi R^2$, and τ_σ and τ_ε are relaxation times.

After characteristic quantities are considered (see Table 1), nondimensional quantities can be introduced in a standard way. The axial velocity u_0 is assumed much larger than the radial velocity v_0, i.e.,

$$v_0 \ll u_0. \tag{2.4}$$

Switching to nondimensional variables, the final equations are obtained through averaging on cross-sections [43,55]. At the wall, the fluid is assumed to move with the vessel. More precisely, if $(r(t), x(t))$ are the coordinates of one particle on the wall of the vessel, then

$$r(t) = R(x(t), (t).$$

After averaging, the continuity equation (2.2) becomes

$$\partial_t A + \partial_x Q = 0, \tag{2.5}$$

where $Q = 2\pi \int_0^R u_x r \, dr$ is the dimensionless flux. Using (2.4) and integrating the r-momentum equation from (2.1) over a cross-section leads to

$$\int_0^R \partial_r p \, r \, dr = 0 \iff p(R, x, t) = \frac{1}{R} \int_0^R p(r, x, t) \, dr \equiv P(x, t).$$

The pressure p is additionally assumed to be independent[4] of r, i.e., $p = P$. The x-momentum equation from (2.1) is now integrated, yielding

$$\partial_t Q + \partial_x \left(2\pi \int_0^R u_x^2 \, r \, dr \right) + A \, \partial_x P = \frac{1}{\mathcal{R}} R \, \partial_r u_x(R, x, t) - \frac{\mathbf{e_x} \cdot \mathbf{k}}{\mathcal{F}} A, \tag{2.6}$$

[3]The assumption of an axisymmetric flow is not strictly necessary to the derivation of models similar to the present one [43].

[4]This is automatically satisfied if $\mathbf{g} = 0$ and/or if $\mathbf{e_r} \cdot \mathbf{e_z} = 0$, with $\mathbf{e_r}$ and $\mathbf{e_z}$ being the unit vectors in the z and r directions, i.e., for a vertical vessel.

with $\mathbf{e_x}$ and $\mathbf{k}$ being the unit vectors in the x and vertical directions, respectively, and where the Froude and Reynolds numbers are defined in Table 1.

To close the model, an additional assumption is needed to relate u_x to the averaged quantities A, Q, and P in terms of which the entire problem will be expressed. Let $U = Q/A$ be the average axial velocity. The axial velocity u_x is sought with the following profile:

$$u_x(r,x,t)=\frac{\gamma+2}{\gamma}U(x,t)\left(1-\left(\frac{r}{R(x,t)}\right)^{\gamma}\right). \tag{2.7}$$

In (2.7), λ determines the profile (for instance, $\lambda = 2$ corresponds to the classical Poiseuille profile; see Figure 2), while the factor $(\lambda + 2)/\lambda$ ensures that the average of u_x is indeed U. The parameter λ is taken as constant = 2 in each vessel in the present study; see the remarks at the end of section 6 for a justification.

The x-momentum equation (2.6) can now be re-expressed in terms of the averaged variables

$$\partial_t Q+\frac{\gamma+2}{\gamma+1}\partial_x\left(\frac{Q^2}{A}\right)+A\partial_x P=-\frac{\gamma+2}{\mathcal{R}}\frac{Q}{A}-\frac{\mathbf{e_x}\cdot\mathbf{k}}{\mathcal{F}}A. \tag{2.8}$$

The system is closed by nondimensionalizing and averaging the Kelvin relation (2.3). Replacing p by P and using the continuity equation (2.5), one finds

$$\partial_t P+\frac{\tau_\varepsilon}{\tau_\sigma}\frac{1}{\mathcal{M}^2}A^{-3/2}\partial_x Q=\frac{1}{\mathcal{W}}(1-P)+\frac{2}{\mathcal{W}\mathcal{M}^2}(1-A^{-1/2}), \tag{2.9}$$

where the Mach and Weissenberg numbers are defined in Table 1 and $c_0=\sqrt{\frac{Eh}{2\rho r_0}}$ is the Moens–Korteweg wave propagation speed; see Table 2.

In summary, the model can be written as

$$(\partial_t+\mathbf{B}\,\partial_x)\begin{bmatrix}A\\Q\\P\end{bmatrix}=\mathbf{G}, \tag{2.10}$$

where

$$\mathbf{B}=\begin{bmatrix}0 & 1 & 0\\ -\frac{\gamma+2}{\gamma+1}\left(\frac{Q}{A}\right)^2 & 2\frac{\gamma+2}{\gamma+1}\frac{Q}{A} & A\\ 0 & \frac{\tau_\varepsilon}{\tau_\sigma}\frac{1}{\mathcal{M}^2}A^{-3/2} & 0\end{bmatrix}$$

and

$$\mathbf{G}=\begin{bmatrix} 0 \\ -\frac{\gamma+2}{\mathcal{R}}\frac{Q}{A}-\frac{e_X k}{\mathcal{F}}A \\ \frac{1}{W}(1-P)+\frac{2}{WM^2}(1-A^{-1/2}) \end{bmatrix}.$$

The eigenvalues of **B** are found to be

$$\lambda_{1,3}=\frac{\gamma+2}{\gamma+1}\frac{Q}{A}\mp\sqrt{\frac{\gamma+2}{(\gamma+1)^2}\left(\frac{Q}{A}\right)^2+\frac{\tau_\varepsilon/\tau_\sigma}{\mathcal{M}^2A^{1/2}}},\quad \lambda_2=0. \tag{2.11}$$

Assuming $A > 0$, the three eigenvalues are real, ensuring the hyperbolicity of (2.10). However, without further assumptions, the sign of $\lambda_{1,3}$, the strict hyperbolicity of the system, and the genuine nonlinearity of the first and third fields cannot be established.

3. Boundary and junction conditions

The vessels forming the circle of Willis are shown in Figure 3; the lengths and diameters of these are given in Table 2. Boundary conditions link the circle of Willis to the cerebral network of smaller arteries and represent the net impedance imposed by the microcirculation. As can be seen from Figure 3, such conditions have to be imposed at the "end" of 9 vessels.

All attempted simulations with realistic parameters have led to two observations:

- $\lambda_1 < 0$, $\lambda_3 > 0$,
- the solutions are smooth.

As a result of the first observation, the resolution of the equations in each vessel requires that one scalar condition has to be enforced at each end of that vessel to ensure well-posedness. The second observation is used below to significantly simplify the treatment of junction conditions.

For three of the vessels (basilar artery as well as left and right internal carotid arteries), inflow conditions are imposed whereby the velocity is prescribed and corresponds to experimental measurements; see section 5. In other words, since the velocity is related to the unknowns through $U = Q/A$, the following conditions will be imposed at the end of the corresponding vessels and at all times:

$$Q_{ves}=\mathcal{U}_{ves}A_{ves},\quad ves\in\{\mathrm{BA},\mathrm{L\,ICA},\mathrm{R\,ICA}\}, \tag{3.1}$$

with the obvious naming convention; see again Figure 1, Figure 3, and Table 2. The velocities U_{ves} in (3.1) are experimentally determined time-dependent functions, and the surface areas are computed from the average radii from Table 2. The remaining conditions are outflow boundary conditions. Those conditions have to mimic the effects of the rest of the vascular system on the circle of Willis. While the issue is delicate and deserves further research, simple ad hoc conditions can be used. In the present work, two such types of conditions are considered. Pure resistance boundary conditions have the form (see, for instance, [60])

$$P_{ves}=R_{ves}Q_{ves},$$
$$ves \in \{\text{L PCA 2}, \text{R PCA 2}, \text{L MCA}, \text{R MCA}, \text{L ACA 2}, \text{R ACA 2}\}. \tag{3.2}$$

Alternatively, boundary conditions based on the three-parameter windkessel model can be used; this model includes two resistors and one capacitor; see, for instance, [2,55,54,57,61]. This corresponds to

$$R^s_{ves}\partial_t Q+\frac{R^s_{ves}+R^p_{ves}}{R^p_{ves}C_{ves}}Q=\partial_t P+\frac{1}{R^p_{ves}C_{ves}}P, \tag{3.3}$$

where, for each vessel *ves* in the same list as in (3.2), R^p_{ves} and R^s_{ves} are resistance parameters and C_{ves} is a compliance parameter.

Junction conditions link vessels to their neighbors. The mathematical derivation of proper junction conditions for systems of conservation laws is nontrivial; it is in fact an active field of research; see, for instance, [10,18,19,42]. The present system of equations (2.10) is not in conservation form, which further complicates the problem. However, as mentioned at the beginning of the section, only smooth solutions are expected (and observed), and thorny questions of selection principles [33,34,32] can be avoided.

Consider a junction J at which N_J vessels intersect. Continuity of the pressure and conservation of the flow are imposed:

$$P_1=P_2=\cdots=P_{N_J},$$
$$\sum_{i=1}^{N_J} Q_i=0, \tag{3.4}$$

where the flux Q_i is counted positive if flowing toward J; see [9, p. 59] for a justification. Other choices have been considered in the literature such as continuity of the total pressure; see [28,49,55,59] for further discussions.

4. Numerical analysis

The equations are discretized in space using Chebyshev collocation methods [14]. Such methods deliver high accuracy with a low number of nodes for smooth solutions (which are expected here). Working in the standard $[-1, 1]$ interval to simplify the notation, Chebyshev collocation is considered at the usual Chebyshev–Gauss–Lobatto nodes:

$$x_j=\cos\left(\frac{\pi j}{N-1}\right),\quad j=0,\ldots,N-1,$$

where N stands for the number of nodes. If v is any of the above unknowns to be determined for $x \in [-1, 1]$ and $t > 0$, we seek an approximation of it of the form

$$v_N(x,t)=\sum_{j=0}^{N-1} V_j(t)\psi_j(x), \tag{4.1}$$

where $\{\psi_j\}_{j=0}^{N-1}$ are the Lagrange interpolation polynomials at the Chebyshev–Gauss–Lobatto nodes on $[-1, 1]$; i.e., $\psi_i(x_j) = \delta_{ij}$, $i, j = 0, \ldots, N - 1$, and the V_j's are time-dependent coefficients to be found. Interpolation on the above nodes of a function $v = v(x, t)$ simply takes the form

$$I_N v(x,t)=\sum_{j=0}^{N-1} v(x_j,t)\psi_j(x).$$

By definition, the Chebyshev collocation derivative of v with respect to x at those nodes is then

$$\frac{\partial}{\partial x}(I_N v)(x_l,t)=\sum_{j=0}^{N-1} v(x_j,t)\psi_j'(x_l)=\sum_{j=0}^{N-1} D_{lj}v(x_j,t),$$

with $D_{lj}=\psi_j'(x_l)$. The collocation derivative at the nodes can be obtained through matrix multiplication by $\mathbb{D}$, which admits the D_{lj}'s as entries.

We introduce the numerical method on a simple advection equation for ease of exposition:

$$\partial_t u + a\,\partial_x u = 0, \tag{4.2}$$

$$u(-1,t)=g(t), \tag{4.3}$$

where $a > 0$ and g is a given function describing the inflow boundary condition. Spatial semidiscretization using the above principles and notation leads to

$$\partial_t u_N + a\,\partial_x u_N = 0.$$

The latter relation is enforced at the internal nodes, and an extra condition is imposed to ensure the verification of the boundary condition (4.3). Typically, that condition is simply[5]

[5]It has been observed that such a condition may lead to both theoretical and practical stability problems (for instance, the structure of the derivative matrix $\mathbb{D}$ is essentially altered [35]). To alleviate these problems, weak implementation of the boundary conditions through a penalty method has been proposed; see [22,35,39]. This type of method has been tested here and was not found to be necessary.

$$u_N(x_{N-1}, t)=g(t).$$

The above method can be applied in a straightforward way to (2.10). Each of the variables *A*, *Q*, and *P* is discretized according to (4.1), leading to the new unknowns A_N, Q_N, and P_N. As said in section 3, the system (2.10) requires two boundary conditions, one at each end of the vessel. With respect to a given junction, this corresponds to a boundary condition for each vessel involved. For illustration purposes, consider a standard vessel bifurcation with one parent vessel and two daughter vessels. Since there are three vessels related to this junction, we will need three boundary conditions. As stated previously, these take the form of (3.4). Thus, in this case, we will have one flow condition and two pressure conditions. This is consistent with the number of conditions needed based on a study of the characteristics of the system.

This results in the following semidiscretized system:

$$\frac{d}{dt}\mathbb{U}+\mathbb{B}(\mathbb{I}_3 \otimes D)\mathbb{U}=\mathbb{G}+\mathbb{F}\left(\mathbb{U}, \frac{d}{dt}\mathbb{U}\right),$$

where $\mathbb{U} = [A(x_0, t), \ldots, A(x_{N-1}, t), Q(x_0, t), \ldots, Q(x_{N-1}, t), P(x_0, t), \ldots, P(x_{N-1}, t)]^T$, $\mathbb{G}$ is the vector obtained in a natural way from $\mathbf{G}_N$ (discretization of **G** from (2.10)), $\mathbb{I}_3$ is the 3 × 3 identity matrix, and ⊗ is the Kronecker product [20]. Finally, all of the contributions from the boundary conditions have been lumped into $\mathbb{F}$, and the matrix $\mathbb{B}$ is defined as

$$\begin{bmatrix} B_{11,0}B_{11,1}\ldots B_{11,N-1}B_{12,0}B_{12,1}\ldots B_{12,N-1}B_{13,0}B_{13,1}\ldots B_{13,N-1}B_{21,0}B_{21,1}\ldots B_{21,N-1}B_{22,0}B_{22,1}\ldots B_{22,N-1}B_{23,0}B_{23,1}\ldots B_{23,N-1}B_{31,0}B_{31,1}\ldots B_{31,N-}$$

with $B_{ij,k} = \mathbf{B}_{N,ij}(x_k)$, where $\mathbf{B}_N$ is the matrix corresponding to the discretization of the matrix **B** in (2.10).

Two different methods have been considered for temporal discretization: a third-order explicit TVD Runge–Kutta method [36,62,63] and a simple backward Euler method. In the first case, the stability of the above numerical approach applied to (4.2), (4.3) (with $g \equiv 0$) was analyzed in [46]. Their stability result (see Theorem 4.2) is "adapted" to an empirical stability condition for the present case. More precisely, the size of the *n*th time step Δt^n is adapted during the calculations and taken as

$$\Delta t^n=\frac{C}{\lambda_\infty(N-1)^2},$$

where λ_∞ is the maximum over all spatial nodes of the spectral radius of the matrix $\mathbf{B}_N$ at the current time and *C* is a constant. However, for the problems at hand, it was observed that the backward Euler method with a limited number of Newton steps as the nonlinear solver was faster overall and leads to results quantitatively comparable to more elaborate TVD solvers. The use of an implicit solver allows us to implement the boundary conditions directly on the primary variables without having to switch to the characteristic variables. Thus, the boundary conditions are implemented by simply removing the appropriate differential equation corresponding to the boundary node and replacing it with an equation for the boundary condition. The results shown below were obtained using the backward

Euler method. After appropriate numerical convergence study, it was determined that solutions computed with as little as four collocation nodes per vessel and two Newton steps per time step are roughly within 5% of the fine mesh solutions.

5. Data analysis

The data analyzed in this study was obtained from one healthy volunteer during rest in the supine position.

Velocity measurements were obtained using digital transcranial Doppler technology[6] using a protocol approved by the Institutional Review Board at the Beth Israel Deaconess Medical Center. The basilar, left and right carotid, and middle anterior and posterior cerebral arteries were insonated using a 2 MHz transducer stabilized using a three-dimensional holder. Recordings were made from the occipital (basilar) and temporal windows (remaining arteries), ensuring a maximal velocity at a given depth (the depth indicates the location of recording within the insonated vessel with respect to the transducer). The Doppler technology uses a power mode to visualize the distance of the recording site from the transducer (depth); see Figure 1(right), top panels. The red color (seen only in the online version) denotes that the flow in the insonated vessel is toward the transducer, and the blue color denotes the flow away from the transducer. The bottom panels show the Fourier spectrum and its envelope, which are used for calculation of blood flow velocity.

Blood pressure was measured using a continuous noninvasive finger arterial blood pressure monitor[7] that reliably tracks intra-arterial blood pressure when controlled for finger position and temperature [53]. Since in this study the subject was in the supine position and the finger was kept at heart level, adjustment for gravity was not needed. In addition, the electrocardiogram (ECG) was measured using standard leads. For each vessel, one-minute continuous recordings of all parameters were gathered. Typical ECG, pressure, and velocity measurements are shown in Figure 4.

All analog signals were recorded at 500 Hz and stored for offline processing.[8] Since measurements were not simultaneous, they include variations in the length of the cardiac cycles. The pressure and velocity data were then postprocessed and aligned using the ECG and equidistantly resampled to a one-second period. A cardiac cycle of 1 second is slightly longer than the average cardiac cycle observed for this subject but within standard values for healthy young people [37].

Geometric measurements of vessel lengths and areas were derived from a magnetic resonance angiogram.[9] The radius and length of the vessels were measured by the software *Medical Image Processing, Analysis, and Visualization* (MIPAV) from the Biomedical Imaging Research Services Section, National Institutes of Health, Bethesda, MD. For each vessel, the diameter was measured at three locations and averaged. Therefore, differences and variations in vessel diameters along the vessel length may not be detected. ICA diameters were computed from a single slice transverse view, while other diameters and vessel lengths were measured from reconstructed three-dimensional images. The accuracy of

[6]PMD 150, Terumo Cardiovascular Systems and Spencer Technologies, Inc., Ann Arbor, MI.
[7]Ohmeda Monitoring Systems, Englewood, CO.
[8]This was done using Labview NIDAQ (National Instruments Data Acquisition System 64 Channel/100 Ks/s, Labview 6i, Austin, TX) on a PC that is currently in use at the SAFE (Syncope and Falls in the Elderly) Laboratory.
[9]Anatomical images of intracranial vasculature were obtained using three-dimensional–MR angiography (time of flight) with the parameters T_E/T_R = 3.9/38 ms, flip angle of 25 degrees, 2 mm slice thickness, −1 mm skip, 20 cm × 20 cm FOV, 384 × 224 acquisition matrix, size 512 × 512, and pixel size 0.39 mm × 0.39 mm at the GE VHI 3 Tesla scanner at the Center for Advanced Magnetic Resonance Imaging at the Beth Israel Deaconess Medical Center.

those geometric measurements is conservatively estimated at ±0.4 mm, based on the image resolution. Averaged lengths and diameters are given in Table 2.

These recordings provided data for our three inflow vessels (the basilar, left, and right carotid arteries) and for the six outflow vessels (the left and right ACA, MCA, and PCA).

The inflow velocity measurements from the BA and ICAs are used to drive the system. With the exception of a small subset used for calibration, the outflow velocity (in MCAs, PCAs, and ACAs) data are used only a posteriori to validate the results. Geometric area data are used to specify the model domain and to determine inflow into the model provided the measured velocity.

Kalman filtering is a recursive algorithm that can be used to optimize parameters in a linear model. It uses model results and data values at each time step to adjust the parameters until the optimal parameters have been found. The model is used to create the model forecast, x^f, and then updated based on available data to create the model analysis, x^a. Specifically, x^a is a weighted linear combination of the state predicted by the model, x^f, and the covariance related to the measurements [23]. This linear combination is determined by the Kalman gain, K, which is central to all types of Kalman filtering.

The matrix K is chosen to minimize the a posteriori error estimate, $x - x^a$, where x is the true state. This is equivalent to minimizing the trace of the analysis error covariance, $P^a = \mathrm{cov}(x - x^a)$. Using the definition of x^a and the properties of covariance and taking the trace of the resulting expression for P^a leads to

$$K = P^f H^T (H P^f H^T + R)^{-1},$$

where P^f is the forecast covariance, H is the measurement operator, and R is the measurement covariance.

When dealing with a nonlinear problem, one can use the extended Kalman filter, which requires the direct calculation of an error covariance matrix at each time step, or the ensemble Kalman filter (EnKF), which approximates the error covariance matrix using an ensemble of states. The EnKF has been used in this work to avoid the costly direct calculation of the error covariance matrix.

To begin, the initial conditions are perturbed in a statistically consistent way in order to form the ensemble of states. At each time step, each of the ensemble members is stepped forward in time, using the model, to create the a priori state estimates. The Kalman gain is then used to create the a posteriori state estimates as weighted averages of the a priori state estimates and the discrepancies between the predicted measurements and the actual measurements [67]. Since the EnKF uses estimates based on the ensemble members to create the Kalman gain, the larger the ensemble size the better the results will be [23].

6. Results

6.1. Calibration

The EnKF has been used to optimize the parameters for both the resistance outflow boundary conditions and the windkessel outflow boundary conditions. In each case, an ensemble size of 100 was used. After processing all the calibration data (an eight period subset of the available data), the final parameter values are considered to be the optimal

values based on the data. The model is then run using the original initial conditions and the optimized parameters, and the results are compared to the data.

Figure 5(top) shows a comparison of the experimental data and the model output using the pure resistance boundary condition in the L MCA over one cardiac cycle. The results using the parameters obtained from the EnKF clearly provide a better fit to the data. Figure 5(bottom) shows a similar comparison, this time with the model results obtained using the windkessel boundary condition. In this case, the original parameters were chosen by adapting the values from [2], and therefore the switch to the EnKF optimized parameters provides less of an improvement. While both boundary conditions yield comparable results, the windkessel results are marginally most accurate.

It is also important to consider the associated pressure data. Since the blood pressure was measured in the finger and not in the brain, the model results are not expected to match the data, but they should be in roughly the same range. Figure 6 shows a comparison of the pressures from the model with the pressures from the data in the L MCA. As expected, the waveforms are not the same, but they are similar.

6.2. Validation

Validation of many blood flow models is limited by the lack of available data and is therefore usually qualitative in nature. Access to clinical data allows the present approach to be validated in a quantitative manner.

Since the cardiac cycle varies over time, even in a single subject, a given set of outflow data is not expected to be matched exactly using a given set of inflow data collected at a different time. Instead, all of the available data is processed, and a mean velocity profile is calculated for each inflow and outflow vessel, along with the associated variances; see the blue and green curves (color only in the online version) in Figures 7 and 8. The available number of measurements, i.e., periods, per vessel varies between 20 and 200.

The simulation is then run with 20 different stochastically perturbed inflow velocity profiles. The inflow conditions are determined by stochastically perturbing the mean change in velocity at each time step to avoid creating artificial roughness in the wave form; the perturbations are drawn from a normal distribution based on the data. The means of the resulting inflow velocities are displayed in Figure 7. The mean predicted velocity in each outflow vessel is compared to the corresponding mean velocity profile from the data; see Figure 8. The breakdown of how well the model results match the data is shown in Table 3. As is evident from both the figures and the table, the model is predicting the velocities at each of the six outflow points consistently.

Figure 9 shows the results of running the deterministic model (where the inflows are taken from the data, not from perturbations of the means) in the L MCA over a number of cardiac cycles. The agreement with the pressure data is expected to only be qualitative since, as explained in section 5, the pressure is measured at a fingertip rather than in the vicinity of the vessels under study.

Some of the physiological parameters used in this study are extremely hard to measure. For instance, no measurements were available for γ which determine the flow profile (see Figure 2) or for the relaxation times τ_{ϵ} and τ_{σ}; see (2.10). While the above results were obtained with $\gamma = 2$, it has been argued that higher values of γ might be more realistic; see, for instance, [12,28], where $\gamma = 9$ is used. Figure 10(top) shows a comparison of the numerical solution in one typical vessel for both $\gamma = 2$ and $\gamma = 9$. In each case, the numerical parameters of the boundary conditions were optimized as done above, while all other physiological

parameters were held constant. The $\gamma = 2$ results are in better agreement with the data. In all previous calculations, the values $\tau_{\in} = \tau_{\sigma} = .125$ are used. Note that having $\tau = \tau_{\in}/\tau_{\sigma} = 1$ roughly corresponds to an elastic model. In Figure 10(bottom), results for $\tau_{\sigma} = .01$ and $\tau_{\in} = .04$ (i.e., $\tau = 4$), which are the values suggested in [65], are compared. It can readily be observed that the value of the ratio τ has very little influence on the velocity. The same was observed for the pressure. For $\tau = 4$, pressure vs. area shows as expected a hysteretic behavior; see Figure 11 for a typical plot. This difference results from changes in the calculated cross-sectional areas. Since we are interested in matching the outflow velocities to those available in the data, viscoelasticity does not seem to play a central role in the present problem.

7. Conclusions

The proposed model and implementation agree remarkably well with the data in spite of their simplicity. A comparison with results from 1.5-dimensional models such as those proposed in [12,13] would be interesting. The present work is in the process of being extended in several directions. First, the method will be used to predict the effects of various pathologies including flow pattern in abnormal circles of Willis from patients with diabetes and for patients with hypertension. Second, while the assumption of Newtonian behavior of the flow is generally considered valid at high shear rates, say over 100 s^{-1}, the observed numerical shear rates are lower here. Non-Newtonian effects can be included through the use of the Cross model; for the viscosity, see, for instance, [1,45];[10] see also [6].

Acknowledgments

The authors are indebted to Jordi Alastruey-Arimon and Darren Wilkinson for valuable discussions and comments. They also thank the referees for many useful comments and criticisms that improved the paper.

The research of the first and fourth authors was partially supported by the National Science Foundation (NSF) through grant DMS-0616597. The second author's research was partially supported by the National Science Foundation (NSF) through grants DMS-0410561 and DMS-0616597.

The third author's research was partially supported by the American Diabetes Association through grant 1-06-CR-25. Both of these authors' research was supported by the National Institutes of Health (NIH) through grants NIH-NINDS R01 NS45745-01A2, 1R41NS053128-01A2, and NIH-NIA-P60 AG8812-11A1 RRCB and by the National Science Foundation (NSF) through grant DMS-0616597.

References

1. Abraham F, Behr M, Heinkenschloss M. Shape optimization in steady blood flow: A numerical study of non-Newtonian effects. Comp Meth Biomech Biomed Eng 2005;8:127–137.
2. Alastruey J, Parker KH, Peiró J, Byrd SM, Sherwin SJ. Modelling the circle of Willis to assess the effects of anatomical variations and occlusions on cerebral flows. J Biomech 2007;40:1794–1805. [PubMed: 17045276]
3. Alnaes MS, Isaksen J, Mardal KA, Romner B, Morgan MK, Ingebritsen T. Computation of hemodynamics in the circle of Willis. Stroke 2007;38:2500–2505. [PubMed: 17673714]

[10] In such a model, the viscosity μ is assumed to be the following function of the strain rate:

$$\mu(\dot{\gamma}) = \mu_{\infty} + \frac{\mu_* - \mu_{\infty}}{(1 + (\lambda\,\dot{\gamma})^{b})^{a}}, \tag{7.1}$$

where $\mu_{\infty} = .0035$ Pa s is the infinite shear viscosity, $\mu_* = .16$ Pa s is the zero shear viscosity, $\lambda = 8.2$ s, $a = 1.23$, $b = .64$, and $\dot{\gamma}$ is the scalar shear rate, i.e., $\dot{\gamma} = \sqrt{2\varepsilon : \varepsilon}$.

4. Alpers B, Berry J. Circle of Willis in cerebral vascular disorders. The anatomical structure. Arch Neurol 1963;8:398–402. [PubMed: 14012272]
5. Alpers B, Berry J, Paddison R. Anatomical studies of the circle of Willis in normal brain. AMA Arch Neurol Psychiatry 1959;81:409–418.
6. Amornsamankul S, Wiwatanapataphee B, Wu YH, Lenbury Y. Effect of non-Newtonian behaviour of blood on pulsatile flows in stenotic arteries. Int J Biomed Sci 2006;1:42–46.
7. Anliker M, Rockwell L, Ogden E. Nonlinear analysis of flow pulses and shock waves in arteries. Z Angew Math Phys 1971;22:217–246.
8. Atabek HB. Wave propagation through a viscous fluid contained in a tethered, initially stressed, orthotropic elastic tube. J Biophys 1968;8:626–649.
9. Azer K, Peskin CS. A one-dimensional model of blood flow in arteries with friction and convection based on the Womersley velocity profile. Cardiovasc Eng 2007;7:51–73. [PubMed: 17566860]
10. Banda MK, Herty M, Klar A. Coupling conditions for gas networks governed by the isothermal Euler equations. Netw Heterog Media 2006;1:295–314.
11. Broderick J, Brott T, Kothari R, Miller R, Khoury J, Pancioli A, Gebel J, Mills D, Minneci L, Shukla R. The Greater Cincinnati/Northern Kentucky Stroke Study: Preliminary first-ever and total incidence rates of stroke among blacks. Stroke 1998;29:415–421. [PubMed: 9472883]
12. Èanic S, Hartley CJ, Rosenstrauch D, Tambaca J, Guidoboni G, Mikelic A. Blood flow in compliant arteries: An effective viscoelastic reduced model, numerics, and experimental validation. Ann Biomed Eng 2006;34:575–592. [PubMed: 16550449]
13. Èanic S, Tambaèa J, Guidoboni G, Mikeliæ A, Hartley CJ, Rosenstrauch D. Modeling viscoelastic behavior of arterial walls and their interaction with pulsatile blood flow. SIAM J Appl Math 2006;67:164–193.
14. Canuto, C.; Hussaini, MY.; Quarteroni, A.; Zang, TA. Spectral Methods in Fluid Dynamics. Springer Ser. Comput. Phys., Springer; New York: 1988.
15. Cebral JR, Castro MA, Soto O, Löhner R, Alperin N. Blood-flow in the circle of Willis from magnetic resonance data. J Engrg Math 2003;47:369–386.
16. Charbel F, Shi J, Quek F, Zhao M, Misra M. Neurovascular flow simulation review. Neurol Res 1998;20:107–115. [PubMed: 9522344]
17. Clark, M.; Kufahl, R. Cardiovascular System Dynamics. MIT Press; Cambridge, MA: 1978. Simulation of the cerebral macrocirculation; p. 380-390.
18. Coclite GM, Garavello M, Piccoli B. Traffic flow on a road network. SIAM J Math Anal 2005;36:1862–1886.
19. Colombo RM, Garavello M. A well posed Riemann problem for the p-system at a junction. Netw Heterog Media 2006;1:495–511.
20. Demmel, JW. Applied Numerical Linear Algebra. SIAM; Philadelphia: 1997.
21. Deparis, S.; Discacciati, M.; Fourestey, G.; Quarteroni, A. *Heterogeneous domain decomposition methods for fluid-structure interaction problems*, in Domain Decomposition Methods in Science and Engineering XVI. In: Widlund, OB.; Keyes, D., editors. Lect Notes Comput Sci Eng. Vol. 55. Springer; Berlin: 2007. p. 41-52.
22. Don WS, Gottlieb D. The Chebyshev–Legendre method: Implementing Legendre methods on Chebyshev points. SIAM J Numer Anal 1994;31:1519–1534.
23. Evensen G. The ensemble Kalman filter: Theoretical formulation and practical implementation. Ocean Dynamics 2003;53:343–367.
24. Fahrig R, Nikolov H, Fox AJ, Holdsworth DW. A three-dimensional cerebro-vascular flow phantom. Med Phys 1999;26:1589–1599. [PubMed: 10501059]
25. Ferrandez A, David T, Bamford J, Scott J, Guthrie A. Computational models of blood flow in the circle of Willis. Comp Meth Biomech Biomed Eng 2000;4:1–26.
26. Ferrandez A, David T, Brown M. Numerical models of auto-regulation and blood flow in the cerebral circulation. Comp Meth Biomech Biomed Eng 2000;5:7–19.
27. Figueroa CA, Vigon-Clementel IE, Jansen KE, Hughes TJR, Taylor CA. A coupled momentum method for modeling blood flow in three-dimensional deformable arteries. Comput Methods Appl Mech Engrg 2006;195:5685–5706.

28. Formaggia L, Lamponi D, Quarteroni A. One-dimensional models for blood flow in arteries. J Engrg Math 2003;47:251–276.
29. Franke V, Parker K, Wee LY, Fisk NM, Sherwin SJ. Time domain computational modelling of 1 D arterial networks in the placenta. M2AN Math Model Numer Anal 2003;37:557–580.
30. Fung, YC. Biomechanics, Mechanical Properties of Living Tissues. Springer; Berlin: 1993.
31. Gerbeau JF, Vidrascu M, Frey P. Fluid-structure interaction in blood flows on geometries coming from medical imaging. Comput & Structures 2005;83:155–165.
32. Godlewski E, Le Thanh K-C, Raviart P-A. The numerical interface coupling of nonlinear systems of conservation laws: II. The case of systems. M2AN Math Model Numer Anal 2005;39:649–692.
33. Godlewski E, Raviart P-A. The numerical interface coupling of nonlinear systems of conservation laws: I. The scalar case. Numer Math 2004;97:81–130.
34. Godlewski E, Raviart PA. A method for coupling non-linear hyperbolic systems: Examples in CFD and plasma physics. Internat J Numer Methods Fluids 2005;47:1035–1041.
35. Gottlieb D, Hesthaven JS. Spectral methods for hyperbolic problems. J Comput Appl Math 2001;128:83–131.
36. Gottlieb S, Shu CW, Tadmor E. Strong stability-preserving high-order time discretization methods. SIAM Rev 2001;43:89–112.
37. Guyton, A.; Hall, J. Textbook of Medical Physiology. 9. W.B. Saunders; Philadelphia: 1996.
38. Henderson K, Eliasziw M, Fox AJ, Rothwell PM, Barnett JM. Collateral ability of the circle of Willis in patients with unilateral carotid artery occlusion. Border zone infarcts and clinical symptoms. Stroke 2000;31:128–132. [PubMed: 10625727]
39. Hesthaven JS. Spectral penalty methods. Appl Numer Math 2000;33:23–41.
40. Hillen B, Drinkenburg BAH, Hoogstraten HW, Post L. Analysis of flow and vascular resistance in a model of the circle of Willis. J Biomech 1988;21:807–814. [PubMed: 3225267]
41. Hillen B, Hoogstraten H, Post H. A mathematical model of the flow in the circle of Willis. J Biomech 1986;19:187–194. [PubMed: 3700431]
42. Holden H, Risebro NH. A mathematical model of traffic flow on a network of unidirectional roads. SIAM J Math Anal 1995;26:999–1017.
43. Hughes TJR, Lubliner J. On the one-dimensional theory of blood flow in the larger vessels. Math Biosci 1973;18:161–170.
44. Kufahl R, Clark M. A circle of Willis simulation using distensible vessels and pulsatile flow. J Biomech Eng 1985;107:112–122. [PubMed: 3999707]
45. Leuprecht A, Perktold K. Computer simulation of non-Newtonian effects on blood flow in large arteries. Comp Meth Biomech Biomed Eng 2001;4:149–163.
46. Levy D, Tadmor E. From semidiscrete to fully discrete: Stability of Runge–Kutta schemes by the energy method. SIAM Rev 1998;40:40–73.
47. Lippert, H.; Pabst, R. Arterial Variations in Man: Classification and Frequency. Bergmann, JF., editor. Verlag; Munich: 1985.
48. Macchi C, Pratesi C, Conti AA, Gensini GF. The circle of Willis in healthy older persons. J Cardiovasc Surg (Toronto) 2005;43:887–890.
49. Matthys KS, Alastruey J, Peiró J, Khir AW, Segers P, Verdonck PR, Parker KH, Sherwin SJ. Pulse wave propagation in a model human arterial network: Assessment of 1-D numerical simulations against in vitro measurements. J Biomech 2007;40:3476–3486. [PubMed: 17640653]
50. Moore SM, David T, Chase JG, Arnold J, Fink J. 3D models of blood flow in the cerebral vasculature. J Biomech 2006;39:1454–1463. [PubMed: 15953607]
51. Moore SM, Moorhead KT, Chase JG, David T, Fink J. One-dimensional and three-dimensional models of cerebrovascular flow. J Biomech Eng 2005;127:440–449. [PubMed: 16060350]
52. Nobile F, Vergara C. An effective fluid-structure interaction formulation for vascular dynamics by generalized Robin conditions. SIAM J Sci Comput 2008;30:731–763.
53. Novak V, Novak P, Schondorf R. Accuracy of beat-to-beat noninvasive measurement of finger arterial pressure using the Finapres: A spectral analysis approach. J Clin Monit 2006;10:118–126. [PubMed: 8207452]

54. Olufsen MS, Nadim A, Lipsitz L. Dynamics of cerebral blood flow regulation explained using a lumped parameter model. Am J Physiol Reg Int Comp Physiol 2002;282:R611–R622.
55. Olufsen MS, Peskin CS, Kim WY, Pedersen EM, Nadim A, Larsen J. Numerical simulation and experimental validation of blood flow in arteries with structured-tree outflow conditions. Ann Biomed Eng 2000;28:1281–1299. [PubMed: 11212947]
56. Pedley, TJ. The Fluid Mechanics of Large Blood Vessels. Cambridge University Press; Cambridge, UK: 1980.
57. Quarteroni A, Tuveri M, Veneziani A. Computational vascular fluid dynamics: Problems, models and methods. Comput Vis Sci 2000;2:163–197.
58. Riggs H, Rupp C. Variation in form of circle of Willis. The relation of the variations to collateral circulation: Anatomic analysis. Arch Neurol 1963;8:24–30.
59. Seeley BD, Young DF. Effect of geometry on pressure losses across models of arterial stenosis. J Biomech 1976;9:439–448. [PubMed: 939765]
60. Sherwin SJ, Formaggia L, Peiró J, Franke V. Computational modelling of 1D blood flow with variable mechanical properties and its application to simulation of wave propagation in the human arterial system. Internat J Numer Methods Fluids 2003;43:673–700.
61. Sherwin SJ, Franke V, Peiró J, Parker K. One-dimensional modelling of a vascular network in space-time variables. J Engrg Math 2003;47:217–250.
62. Shu CW. Total-variation-diminishing time discretizations. SIAM J Sci Statist Comput 1988;9:1073–1084.
63. Shu CW, Osher S. Efficient implementation of essentially non-oscillatory shock-capturing schemes. J Comput Phys 1988;77:439–471.
64. Steele BN, Olufsen MS, Taylor CA. Fractal network model for simulating abdominal and lower extremity blood flow during resting and exercise conditions. Comp Meth Biomech Biomed Eng 2007;10:39–51.
65. Valdez-Jasso, D.; Haider, MA.; Banks, HT.; Bia, D.; Zocalo, Y.; Armentano, R.; Olufsen, MS. IEEE Trans Biomed Eng. Analysis of viscoelastic wall properties in ovine arteries. to appear
66. Viedma A, Jimenez-Ortiz C, Marco V. Extended Willis circle model to explain clinical observations in periorbital arterial flow. J Biomech 1997;30:265–272. [PubMed: 9119826]
67. Welch, G.; Bishop, G. An Introduction to the Kalman Filter, Technical report TR-95-041. University of North Carolina at Chapel Hill; Chapel Hill, NC: 2006. http://www.cs.unc.edu/~welch/kalman/kalmanIntro.html

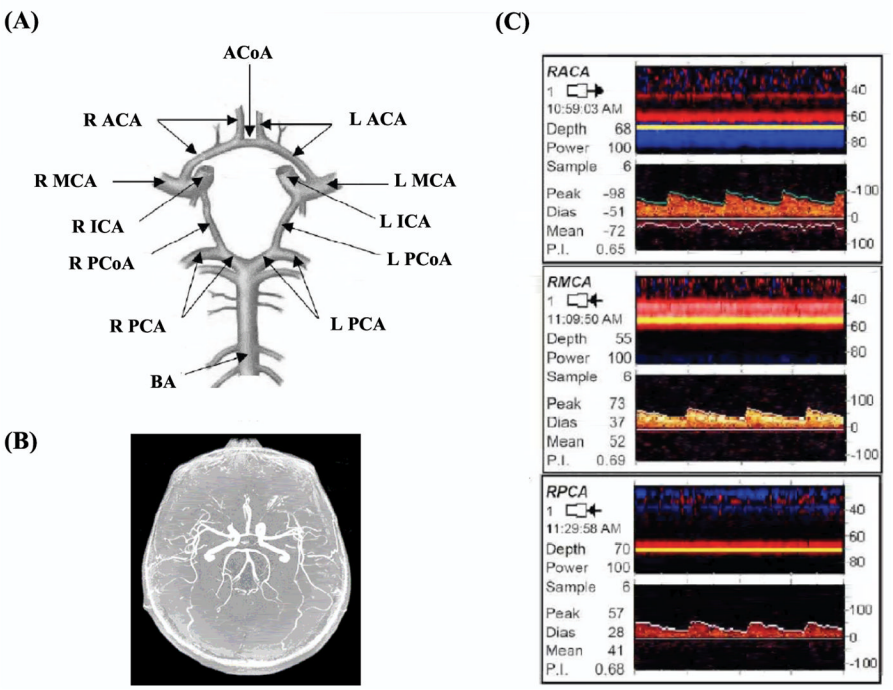

Fig. 1.

(A) Structure of the circle of Willis basilar artery (BA); right posterior cerebral artery (R PCA), left posterior cerebral artery (L PCA), right posterior communicating artery (R PCoA), left posterior communicating artery (L PCoA), right internal carotid artery (R ICA), left internal carotid artery (L ICA), right middle cerebral artery (R MCA), left middle cerebral artery (L MCA), right anterior cerebral artery (R ACA), left anterior cerebral artery (L ACA), anterior communicating artery (ACoA); (B) time of flight magnetic resonance angiography of the circle of Willis; (C) blood flow velocities measurements obtained by transcranial Doppler ultrasound for the right anterior cerebral artery (R ACA), right middle cerebral artery (R MCA), and right posterior cerebral artery (R PCA).

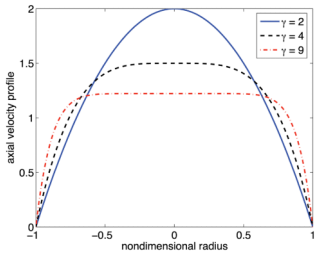

Fig. 2.
Velocity profiles corresponding to (2.7) $\lambda = 2$ (Poiseuille), $\lambda = 4$, and $\lambda = 9$.

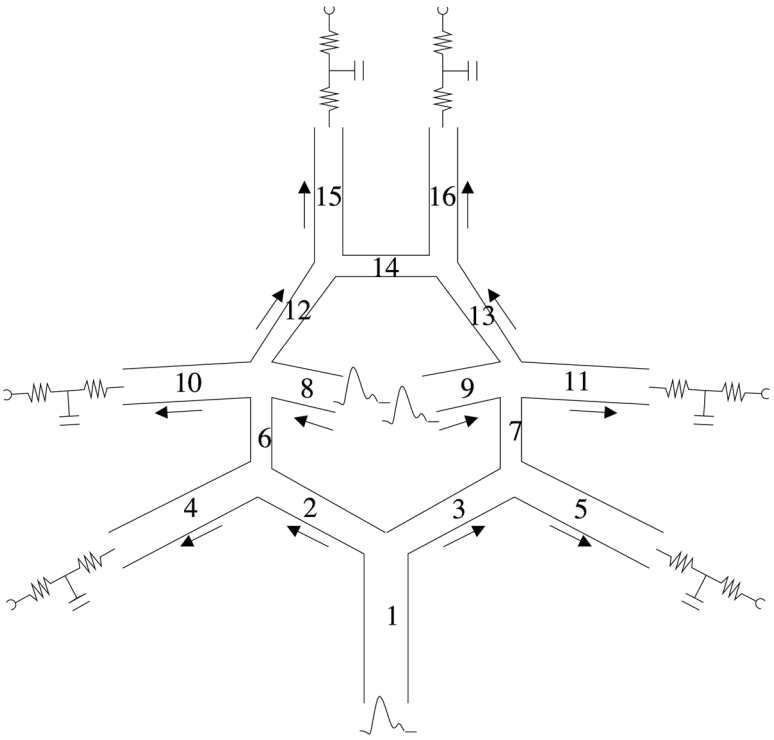

Fig. 3.
Topology of the circle of Willis and numbering convention (see also Figure 1 and Table 2); inflow conditions are marked with a wave, while outflow conditions are marked with a windkessel circuit with two resistors and a capacitor.

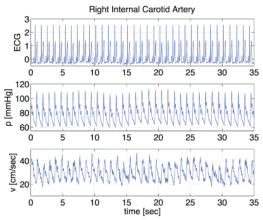

Fig. 4.
Typical raw data file: top graph shows the ECG; middle graph shows finger blood pressure *p*; and bottom graph shows blood velocity in the R ICA.

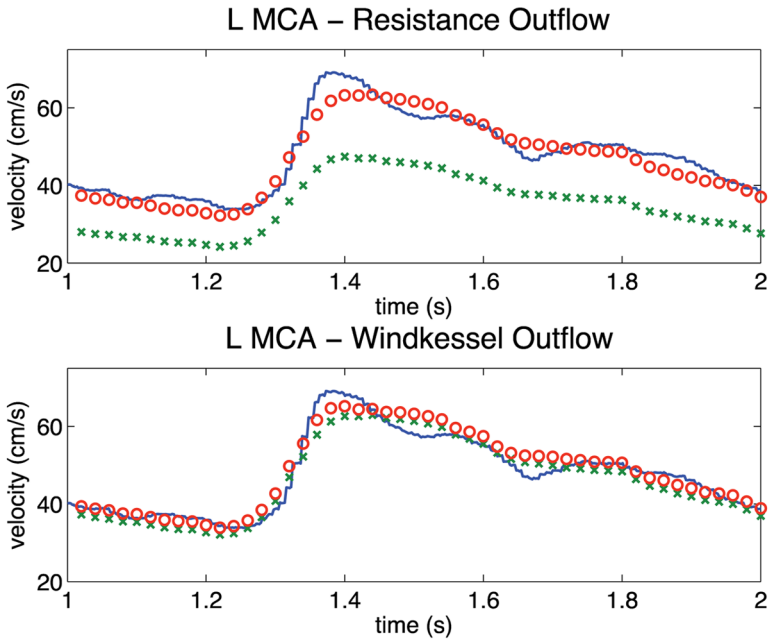

Fig. 5.

Comparison of model velocity results to velocity data in the L MCA using (top) the resistance outflow boundary condition and (bottom) the windkessel outflow boundary condition; solid (blue) line: data, *x*: model-original resistance parameters, ○: model-EnKF optimized resistance parameters.

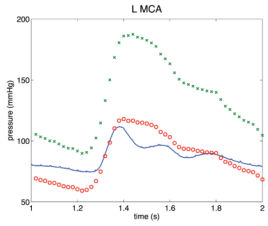

Fig. 6.

Comparison of model blood pressures to data before and after running the EnKF; solid (blue) line: data, *x*: model-original resistance parameters, ○: model-EnKF optimized resistance parameters.

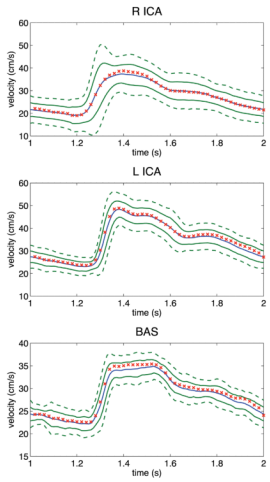

Fig. 7.
Mean inflow velocities used to run the stochastic version of the model; blue line: μ, green line: $\mu \pm \sigma$, dashed line: $\mu \pm 2\sigma$, x: resulting mean inflows.

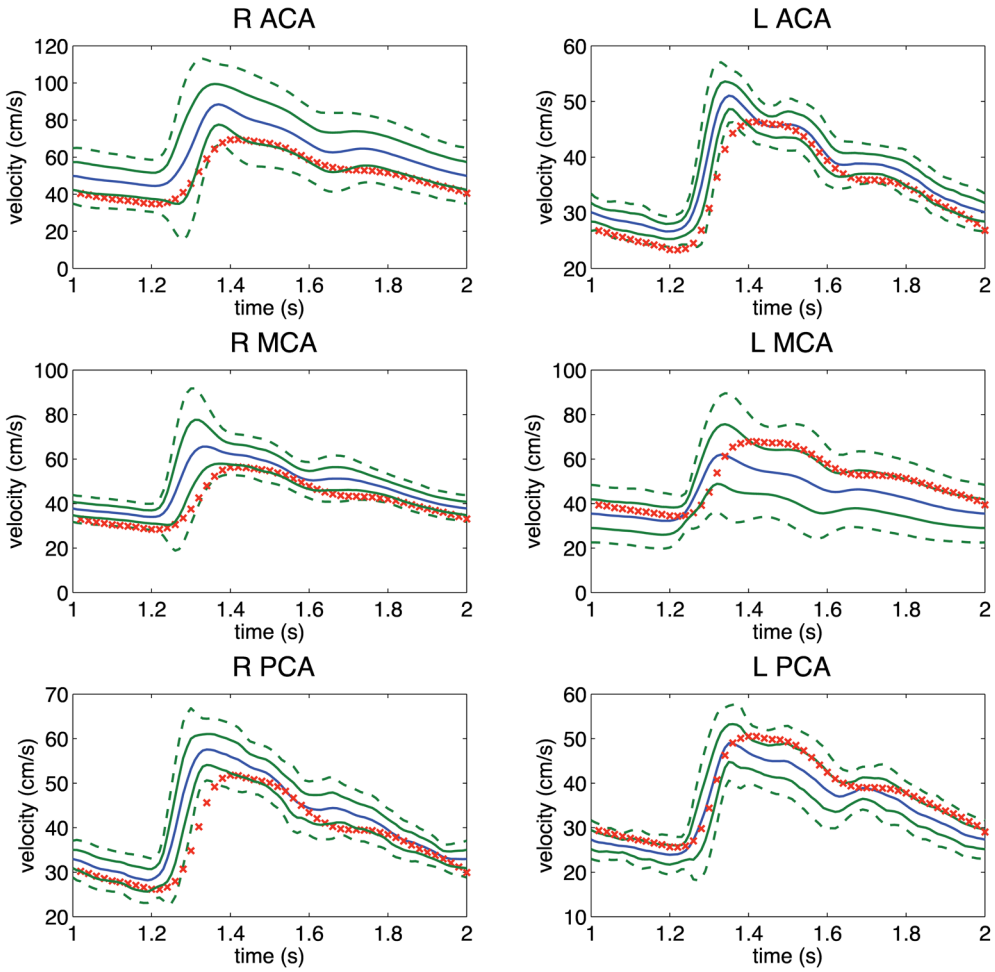

Fig. 8.

Mean outflow velocities resulting from running the stochastic version of the model over [20] realizations; blue line: μ, green line: $\mu \pm \sigma$, dashed line: $\mu \pm 2\sigma$, x: mean predicted outflow.

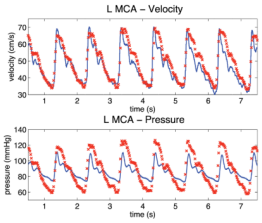

Fig. 9.
Comparison of model results to data in the L MCA over multiple cardiac cycles; solid line: data, *x*: predicted outflow.

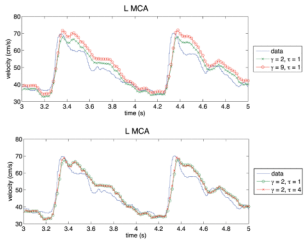

Fig. 10.

Comparison of model results to data in the L MCA over two cardiac cycles. Top: influence of γ; bottom: influence of the relaxation times τ_σ and τ_ϵ ($\tau = \tau_\epsilon/\tau_\sigma$).

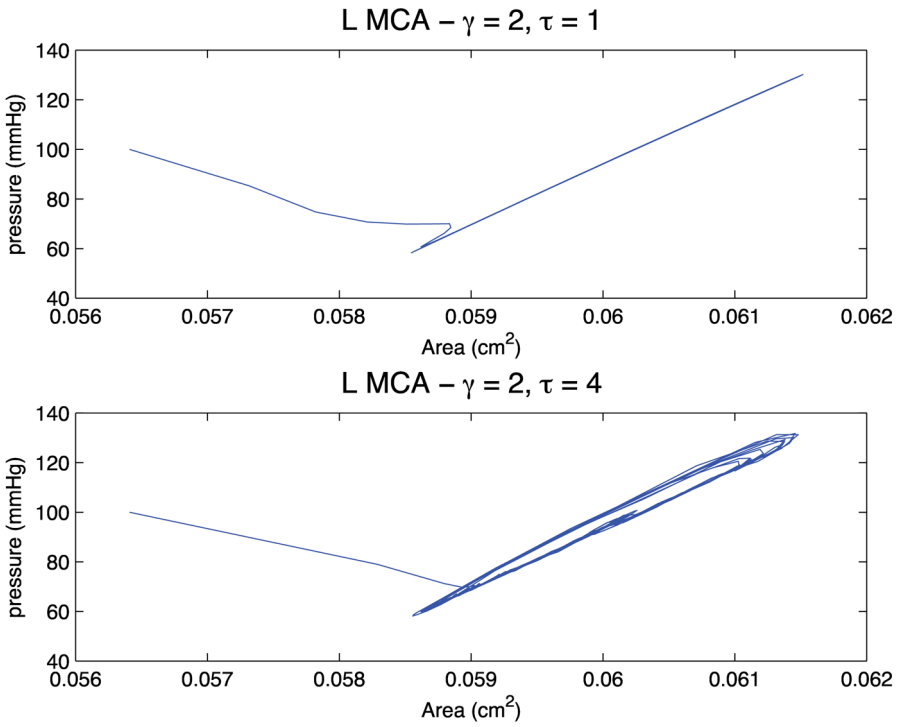

Fig. 11.

Pressure vs. area behavior for L MCA with $\tau = 1$ (essentially elastic), top, and $\tau = 4$ (viscoelastic), bottom. The "tails" correspond to the initial condition; time goes from $t = 0$ to 8 s as in Figure 9.

Table 1

Characteristic quantities and nondimensional parameters.

Characteristic quantities			
flow:	q_0	axial velocity:	$u_0=\frac{q_0}{A_0}$
radius:	r_0	length:	$x_0=\frac{r_0 u_0}{v_0}$
radial velocity:	v_0	time:	$t_0=\frac{r_0}{v_0}=\frac{x_0}{u_0}$
surface area:	$A_0=\pi r_0^2$	pressure:	$p_0=\rho u_0^2$
Nondimensional parameters			
Reynolds number:	$\mathcal{R}=\frac{\rho r_0 v_0}{2\pi\mu}$	Froude number:	$\mathcal{F}=\frac{u_0 v_0}{g r_0}$
Weissenberg number:	$\mathcal{W}=\frac{\tau_\sigma v_0}{r_0}$	Mach number:	$\mathcal{M}=\frac{u_0}{c_0}$

Table 2

Physiological data used in the calculations (see Figure 3 for the naming conventions). The * values were missing from the measurements and had to be estimated from the literature [2]. The Moens–Korteweg wave propagation speed $c_0 = \sqrt{\frac{Eh}{2\rho r_0}}$ is computed under the assumption $h = r_0/4$.

	Name	Diameter (mm)	Length (mm)	E (10^6 g/s ^{2}cm)	c_0 (10^2 cm/s)
1	BA	3.0	8.2	8.0	9.7
2	R PCA 1	2.2	3.3*	16	14
3	L PCA 1	2.2	3.3*	16	14
4	R PCA 2	2.2	7.6	16	14
5	L PCA 2	2.2	7.6	16	14
6	R PCoA	2.0	10*	16	14
7	L PCoA	2.0	10*	16	14
8	R ICA	4.2	48	8.0	9.7
9	L ICA	4.2	48	8.0	9.7
10	R MCA	2.7	21	16	14
11	L MCA	2.7	21	16	14
12	R ACA 1	3.4	11	16	14
13	L ACA 1	2.0	11	16	14
14	ACoA	2.0	2.0	16	14
15	R ACA 2	2.3	23	16	14
16	L ACA 2	2.3	23	16	14

Table 3

Percentage of time the model mean is within one or two standard deviations (σ) of the data mean (μ) in each of the six outflow vessels.

	% within $(\mu - \sigma, \mu + \sigma)$	% within $(\mu - 2\sigma, \mu + 2\sigma)$
R PCA	66	90
L PCA	48	100
R MCA	16	100
L MCA	54	100
R ACA	32	98
L ACA	40	84